Article:
Nourafkan, E, Asachi, M, Gao, H et al. (2 more authors) (2017) Synthesis of Stable Iron Oxide Nanoparticle Dispersions in High Ionic Medi. Journal of Industrial and Engineering Chemistry, 50. pp. 57-71. ISSN 1226-086X

https://doi.org/10.1016/j.jiec.2017.01.026

Title: Synthesis of Stable Iron Oxide Nanoparticle Dispersions in High Ionic Medi

Authors: Ehsan Nourafkan, Maryam Asachi, Hui Gao, Ghulum Raza, Dongsheng Wen

PII: S1226-086X(17)30042-4
DOI: http://dx.doi.org/doi:10.1016/j.jiec.2017.01.026
Reference: JIEC 3270

To appear in:

Received date: 16-9-2016
Revised date: 27-12-2016
Accepted date: 22-1-2017

Please cite this article as: Ehsan Nourafkan, Maryam Asachi, Hui Gao, Ghulum Raza, Dongsheng Wen, Synthesis of Stable Iron Oxide Nanoparticle Dispersions in High Ionic Medi, Journal of Industrial and Engineering Chemistry http://dx.doi.org/10.1016/j.jiec.2017.01.026

Synthesis of Stable Iron Oxide Nanoparticle Dispersions in High Ionic Medi

Ehsan Nourafkan[1], Maryam Asachi[1], Hui Gao[1], Ghulum Raza[1], Dongsheng Wen[1,2*]

[1]School of Chemical and Process Engineering, University of Leeds, Leeds, LS2 9JT, U.K.

[2]School of Aeronautic Science and Engineering, Beihang University, 100191, P.R.China

Email: d.wen@leeds.ac.uk

Graphical abstract

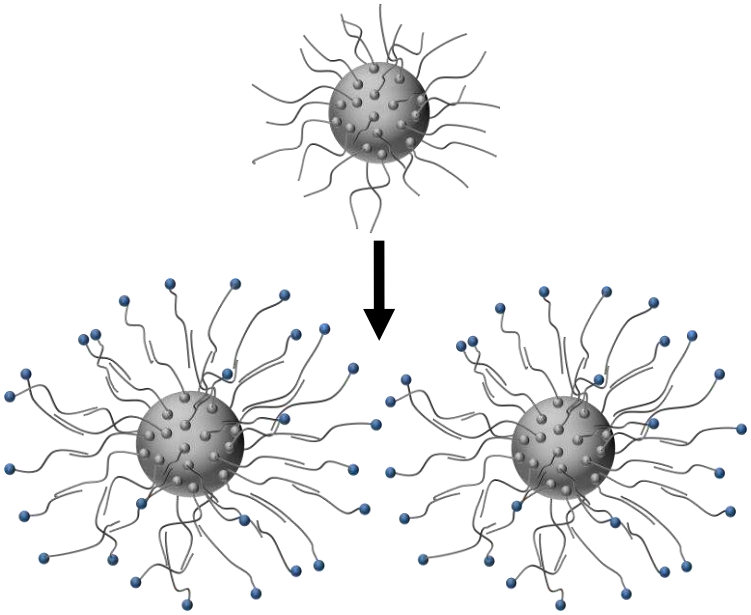

ABSTRACT

A novel one-pot method was developed in this work to synthesize and disperse nanoparticles in a binary base fluid. As an example, stable magnetite iron oxide (Fe_3O_4) dispersions, i.e., nanofluids, were produced in a high ionic media of binary lithium bromide-water using a microemulsion-mediated method. The effects of temperature and precursor concentration on morphology and size distribution of produced nanoparticles were evaluated. An effective steric repulsion force was provided by the surface functionalization of nanoparticles during the phase transfer, supported by the Derjaguin-Landau-Verwey-Overbeek (DLVO) theory. The formed nanoparticles exhibited a superior stability against agglomeration in the presence of high concentrations of lithium bromide, i.e., from 20 to 50 wt.%, which make them good candidates for a range of novel applications.

Keywords: Iron oxide nanoparticles, lithium bromide, binary nanofluid, reverse microemulsions, ionic media, DLVO theory.

Introduction

Formulating stable nanoparticle dispersions (i.e. nanofluids) are fundamental to a wide range of applications, from materials processing, chemical reactions to heat transfer intensifications [1, 2]. Most of the formation processes are based on a two-step method [3]. In this method, nanoparticles need to be produced first, followed by complicated processes including particle purification, separation, drying, packaging and storage, which produced many agglomerations. Such particles are then dispersed into a base fluid under suitable ionic or surfactant conditions

[4]. Considering the close relationship between the structures and properties, the dispersed status of nanoparticles in the fluid plays a crucial role in determining the effective properties of the dispersion. The one-step method, which produces and disperses nanoparticle into the required fluid simultaneously, looks very appealing. Most of the one-step methods have been focused on dispersing particles into a single base fluid [3].

Microemulsions have recently received intensive interest for the synthesis of nanomaterials. The nanodroplets inside a microemulsion behave as energetic barriers that prevent ion-ion encounters of the precursors and surfactants around droplets, contributing to the steric stabilization of droplets [5]. Some surfactant molecules inside the droplets can also affect the growth of different facets of nanoparticles, leading to the production of particles with different morphologies and improved stabilities [6]. Different particle morphologies including spheres, rods and disks can be produced by properly adjusting the controlling parameters such as surfactant concentration, mole ratio of water to surfactant, oil and co-surfactant, and reaction temperature [7-9]. Such versatility makes microemulsion a promising method to produce particles with controlled size, shape, homogeneity, stability and functionalizing surface area. Microemuslisons have been successfully used to produce different iron oxide nanoparticles [10-12]. The research regarding the synthesis of stable nanoparticles in a high ionic media of lithium bromide (LiBr) solution, however, has never been reported.

Binary fluids have many unique applications in a variety of fields. For instance, LiBr-water binary is an effective working medium for absorption refrigeration systems and is suitable for many solar-based applications including solar thermal air conditioning [13, 14]. It has been reported that dispersing suitable nanoparticles into a base fluid can trap more solar light energy and improve significantly the system energy efficiency [15]. Among various particles investigated, Alfaro et al. [16] experimentally showed that iron oxide nanoparticles were very promising in absorbing solar energy. However the stability of nanoparticles in a high ionic media of LiBr is a big challenge. The challenge lies on the dominance of the combined magnetic and van der Waals attractive forces. Simply relying on the steric repulsion force in the ionic media, where electrostatic double layer (EDL) repulsions are insignificant, is difficult to achieve the stabilization. The ionic media would compress the EDL around nanoparticles and cause the formation of aggregates. Formulating stable nanoparticle dispersion in an ionic binary fluid

becomes a key issue to advance its applications. Sesen et al. produced high stable super paramagnetic iron oxide nanofluids by functionalizing particles with a bilayer of lauric acid [17]. The experimental results showed that this type of nanofluids were able to improve heat transfer under both single and two phase conditions, and the stability of nanofluids could be improved by applying magnetic actuation [17, 18]. There were a few prior studies investigated the stability of iron oxide nanoparticles in ionic strength media [19, 20], but focused on the short term effect, i.e., a few days.

In this study, we present a novel one-pot microemulsion method to synthesize iron oxide nanoparticles with a narrow size distribution and robust surface functionalization. The proposed method provides a facile functionalizing strategy for separating nanoparticles from the oil phase. The functionalization includes the formation of a bi-ligand surfactant around nanoparticles during the phase transfer of nanoparticles from the oil phase to water phase after the reaction inside microemulsions. The bi-ligand layers serve as excellent steric stabilizers to prevent the flocculation and aggregation of nanoparticles. The long term stability of nanoparticles was analyzed in binary base fluids containing 20, 30, 40 and 50 wt.% LiBr salt and the results confirmed the prosperity of our new synthesis method. Investigation the effect of temperature and precursor concentration on the morphology change is another aspect of novelty in current research.

Materials and Experimental Methods

Materials and Characterization

Analytical grade materials including cyclohexane, sorbitanemonooleate (Span 80, HLB=4.3), polyethylene glycol sorbitanmonolaurate (Tween 80, HLB=15), propyl alcohol, sodium hydroxide, ferric chloride ($FeCl_3$), ferrous chloride ($FeCl_2$), LiBr and citric acid were purchased from Sigma-Aldrich and used without further processing.

The morphology and size distribution of produced Fe_3O_4 nanoparticles were analyzed by Transmission electron microscope (FEI Tecnai TF20 TEM). High resolution TEM (FEI Titan Themis 300), which is equipped with super-X EDX system with 4-detector, was used to study

the crystal lattice and elemental composition of nanoparticles. Zeta potential and hydrodynamic size of nanofluids was analyzed using Malvern Zetasizer Nano-ZS (Malvern Instruments, UK) and the measurement of UV/visible absorption spectra of nanoparticles was performed by a UV 1800-spectrophotometer (Shimadzu Corporation, Japan). The stability of nanoparticles over flocculation and sedimentation was characterized by a dispersion analyzer centrifuge (LUMiSizer 6110, Lum GmbH, Berlin, Germany). Varian 240FS atomic absorption spectrophotometry (Varian Ltd, USA) was applied for the determination of iron oxide concentration.

Synthesis of Iron Oxide Nanoparticles

Based on our previous experience [21], water/cyclohexane/Span 80-Tween 80/isopropyl alcohol were selected to form reverse microemulsions with the minimum average droplet size and polydispersity. The Massart co-precipitation method was used for the production of magnetite nanoparticles according to the following reaction [22]:

$$FeCl_2 + 2\,FeCl_3 + 8NaOH \rightarrow Fe_3O_4 + 8NaCl + 4H_2O \quad (1)$$

Table 1 shows the concentration and temperature condition of several experiment runs. The concentrations of other components were prepared based on chemical stoichiometry with ferrous chloride.

The reverse microemulsion was prepared by mixing 1 ml of deionized water containing $FeCl_3$and $FeCl_2$ with a mixture of 8 ml cyclohexane, 0.05 g Span 80-0.45 g Tween 80 and 0.5 ml propyl alcohol for 1 hour under magnetic stirring. One ml of sodium hydroxide solution as the precursor was added drop wise to the reverse microemulsion for a period of 10 minutes. The mixture was stirred over 4 hours to reach the equilibrium. A trial was performed without using any surfactant in the mixture to compare with the reverse microemulsion method.

Results and Discussion

Separation of Nanoparticles

Fig. 1(a) shows the image of the final reactant dispersions for different experimental runs. The change in the color of final dispersion suggests the presence of different sizes of Fe_3O_4 nanoparticles. One trial was done with a water/alcohol/cyclohexane system without using any surfactant (Fig. 1(b)). The black color and adsorption of the suspension by a magnet show the formation of a magnetic fluid with large particle size.

In order to separate Fe_3O_4 nanoparticles from the reaction dispersion, a neodymium-samarium cobalt magnet (18 kg pull force) and a centrifuge (Thermo Scientific megafuge 16R) were tried. The dispersions were centrifuged for 30 minutes at the speed of 13000 rpm. The comparison of the results before and after showed a negligible effect of the centrifugation effect on the separation of nanoparticles. Also, the efficiency of separation by a strong magnet was too low to have a good separation. The small size of nanoparticles and functionlisation with surfactants show a great resistance of nanoparticles against separation by a centrifuge or magnet [23].

Phase Transformation of Nanoparticles

Phase transformation is another strategy for the separation of nanoparticles. During the phase transformation, the ligands on the surface of nanoparticles are modified to generate new binding ligands. The work of Sperling and Parak [24] showed that such modification could transfer the formed nanoparticles from the original nonpolar environment (i. e., organic phase) to a polar aqueous phase. In addition, the presence of ligand could also provide the colloid with an increased stability, e.g. by exchanging hydrophobic with the hydrophilic ligands.

Similar strategy was used in our experiments. Fig. 2(a) shows the dispersion of nanoparticles in an organic phase after the separation of reverse microemulsion in Case 2. By adding some droplets of acetic acid to the dispersion, iron oxide nanoparticles were transferred to the water phase (Fig. 2(b)). As schematically illustrated in Fig. 2(c), surfactant covers iron oxide nanoparticles with the hydrophilic head group and the hydrophobic tails cause the nanoparticles to disperse in cyclohexane.

The addition of acid may add a new layer of surfactant molecules on the original ligand of nanoparticle surface, which changes the hydrophobicity to hydrophilicity [24]. The validity of

this mechanism was checked by measuring the hydrodynamic size of iron oxide nanoparticles by the dynamic light scattering (DLS) method. Fig. 3(a) presents the DLS result of iron oxide nanoparticles in Case 2, which was obtained after the evaporation of cyclohexane. The average hydrodynamic size of particles in this sample was equal to 8.91±0.39 nm. Fig. 3(b) represents the DLS result of iron oxide nanoparticles in Case 2 after the addition of acid citric and the separation of aqueous phase. The average hydrodynamic size was 13.8±0.98 nm. The 4.4 nm increment in size was probably due to the formation of admicelles around the nanoparticles, as shown schematically in Fig. 2(c).

The concentration of LiBr in the absorption refrigeration system is varied within (10-50%), and these values differ from one design to another. Moreover in the same system, the concentration varies from the generator and the absorber [25, 26]. In this study, LiBr/water nanofluid was produced after the phase transformation of nanoparticles, separation of water phase and addition of 30 ml extra ionized water containing different concentrations of LiBr (20, 30, 40 and 50 wt.%). Fig. 4 shows the final nanofluids for different experimental runs. The concentrations of iron oxide nanoparticles were measured by atomic adsorptions which were provided in Table 2.

In order to evaluate the efficiency of proposed one-pot method, the oil phase was separated and reused for nanoparticle synthesis. For this purpose, the above oil phase for Case 6 (Fig. 2(b)) was separated from the aqueous phase. The weight of recovered oil was 6.8 g, which showed 85 % recovery of oil phase. It is expected that with further improvement of the facility in large scale process, the recovery percent can be increased. Nanoparticles were synthesized again according to “Synthesis of Iron Oxide Nanoparticles” section and conditions of Case 6. Just instead of pure cyclohexane, the recovered oil phase was used.

TEM and UV-visible Analysis

Fig. 5 shows the TEM images of iron oxide nanoparticles prepared under different conditions. It is clear that prepared iron oxide nanoparticles were spherical at low reactant concentrations while the morphology was shifted to rod shape by increasing the concentration. The fraction of spherical nanoparticles was higher in samples produced in room temperature. The

increase of temperature increased the tendency of nanoparticles to be converted into rod morphology. The reasons for this morphology change will be described in section 3-4.

Image processing is one of the accurate methods for size distribution evaluation [27, 28]. For instance, Gontard et al proposed a simple algorithm for the measurement of nanoparticles size distribution using image processing [29], and found that the proposed method had greater accuracy for particle characterization than the conventional methods. Photoshop software was used for analysis images in different scientific topics (e.g. medical, food, engineering) as robust image processing software [30-32]. In this study, the size distribution of nanoparticles was estimated from at least 100 nanoparticles via image processing of TEM photos by photoshop 7 software, which is illustrated in Fig. 6. The equivalent size and aspect ratio of rod shape nanoparticles were calculated by following equation:

$$D_e = \sqrt{\frac{4.A.S^2}{\pi.P_S}}$$
$$AS = \frac{\text{Size of longer side}}{\text{Size of shorter side}} \quad (2)$$

where AS is aspect ratio (-), D_e is equivalent size (nm), S is length of scale bar of TEM photo (nm), A is total pixel area of a single nanoparticle (#) and P_s is total pixel area of a square ($S \times S$) on TEM photo calculated by photoshop software. Table 2 represents the average size and polydispersity index of nanoparticles which were synthesized at different runs.

Fig. 7 shows the TEM images of nanoparticles which were synthesized using the recovered oil phase, after second phase separation. The average size and polydispersity index of rod shaped nanoparticle based on TEM image was estimated as 12.88 nm and 0.026 respectively. The average size is near to case 6 (Table 2), which shows the ability of recovered oil phase for once nanoparticle synthesis.

Fig. 8 illustrates the UV/visible absorption spectra of final reactant dispersion of different experimental runs. The shift of UV spectra to right side is because of increasing concentration of iron oxide nanoparticles in different cases; however the change of morphology also affect on adsorption spectra. The adsorption band of spectra shows the excellent capability of iron oxide

nanoparticles in the visible light spectrum, especially the rod shaped particles with large aspect ratios, which is promising for potential photo-thermal conversion applications [33].

Proposed Formation Mechanism of Nanoparticles with Different Morphologies

Several researchers have observed the effect of surfactant type [34, 35], changing temperature or concentration of reactants on the morphology of nanoparticles [36, 37]. Fig. 10(a) shows the formation of iron oxide nuclei in a reverse microemulsion droplet. The sodium hydroxide agent converts Fe^{3+} and Fe^{2+} into iron oxide atoms inside droplets. At low concentrations, these oxides present as spherical nuclei, inside droplets, and the growth is limited due to low number of atoms, leading to the production of small spherical particles inside the droplets (i.e. Case 1). Further increase of reactant concentration leads to an increase of the ion occupancy and iron oxide atoms formation per reverse droplet, which promotes the growth of spherical nuclei.

As the surface energies of crystal facets are different, the capping agents such as surfactants can bind specifically to particular facets, hence lowering the surface energy [38]. For instance, usually surfactants prefer to attach on the (100) facet rather than (111) facet, which leads to an ordered anisotropic growth to produce nanorods particle [39, 40]. Crystallography of Fe_3O_4 naanoparticles are inverse-spinel crystal with face-centered cubic, structures (Fd3m space group) [41]. Several work have reported the elongation of magnetite iron oxide crystal based on (110) plan [42-44], (100) plan [45, 46], and (111) plan [47, 48], which formed nanorods morphology. Wang et al. observed a lattice spacing of 0.48 nm for Fe_3O_4 nanorods particles in HRTEM image which is in agreement with the distance between the (111) lattice planes and confirmed the preferred growth direction was (110) [49]. On the other hand, Mathur et al. and Han et al. observed lattice spacing of 0.298 nm, which match well with the (220) lattice planes and confirmed that the nanorods grew along (110) direction [50, 42]. Fig. 9 shows our HRTEM images and EDEX analysis of spherical and rod shaped iron oxide nanoparticles. According to HRTEM, the lattice planes was measured equal 0.29 nm, which shows (110) plan as a preferred growth direction for iron oxide nanoparticles. EDEX analysis of rod shaped iron oxide nanoparticles showed a strong peak in graph at 6.4 keV (Fig. 9(d, e)) corresponding to the iron

element. An extra peak of carbon and cupper were observed on EDEX graph, which was due to the carbon coated copper TEM grids used.

It was observed that some specific surfactant blend systems have greater performance than the individual surfactant [51, 52]. Bera et al. [53] showed that nonionic/cationic surfactant mixtures have lower surface tension than nonionic/anionic surfactant mixture due to a synergistic effect. The synergistic effect of surfactant blend is due to the contributions of surfactant's headgroup, which enhance one another performance. Generally, this synergistic effect produces more compact micelles with smaller size. Posocco et al. [54] also revealed a significant synergistic effect between Tween-Span surfactants molecule. They showed that low molecular weight Span molecules occupied free spaces between the much larger, bulky Tween compounds. Similarly, in our case the Span-Tween surfactant molecules inside the water droplets began covering, via adsorption or selective bonding, to the specific facets of iron oxide nanoparticle, which modified the surface growth rate (Fig. 10(b)). A selective adsorption/bonding on preferred facets (110) would provide some surface passivation selectively, blocking some reaction sites. The facet which possesses higher surface energy was eliminated during the growth while the facet with more tightly packed surfactant layer had less participation in the spherical nuclei growth. This would lead to a directional growth of crystal along [110] plan, which lead to the formation of rod shaped particle as schematically shown in Case 3.

An increase of the reaction temperature also promoted the formation of rod-shaped particles (i.e. Case 4 and 5), which shall be caused by three main reasons. Firstly, with the increase of the temperature, the vibration energy of surfactant molecules at oil/water interface increases, which lead to their separation from interface and movement to oil or water bulk phase. Therefore the rigidity of reverse droplets interface would be decreased, which is further promoted by the shear rate direction during the mixing (Fig. 10(c)). The tendency of deformation of water droplets in specific direction is advantageous for the growth of the nuclei along its preferential direction (i.e.,[110] path). Secondly, an increase in temperature will increase the rate of formation iron oxide reaction by increasing the fusion and fission of water droplets, leading to elongated droplets. Finally the higher temperature helps the completion of iron oxide crystalline state by increasing the reaction rate. A combination of a high concentration and high temperature produced the iron oxide nanoparticles with the largest aspect ratios, showing the best absorption

capability, especially in the visible light spectrum, Fig. 8. Similar observation on the effect of temperature was also reported by Li et al., [55] who reported a morphology change from a sphere into a rod-like shape for TiO_2 nanoparticles at higher temperature.

Stability Analysis

As a direct and absolute technique it requires no calibration or measurements of standards. Analytical centrifugation as a direct and absolute technique, is a powerful technique for the characterisation of nanoparticles in colloidal systems [56]. For instance, Chiu et al. showed that the results of LumiSizer were comparable with those obtained using dynamic light scattering, scanning electron microscope and zeta potential analysis [57]. In this study, a dispersion analyzer (LUMiSizer 6110) instrument was used to determine the stability of LiBr nanofluids. The stability was analyzed by recording the transmission of near-infrared light during centrifugation of nanofluid. The variation of the light extinction curves after centrifugal provided a qualitative description, a rigorous formulation can provide detailed quantitative characterization.

The iron oxide dispersion in LiBr nanofluids (0.5 ml) was filled in a polycarbonate capillary cell and centrifuged for about 3 h (255 profile and 44 interval) at 3150 rpm (light factor 1, 25 ºC, 870 nm NIR LED), which is equivalent to 6 months in real conditions. The correlation between real time and centrifuge time is presented in "Calculation of the total measurement time for LUMiSizer 6110" part of supplementary document. The stability analysis was performed three times for nanofluid without LiBr to evaluate the repeatability. The results were represented in Table 3 and supplementary document (Repeatability of Lumisizer analysis part). The results of repeatability showed the validity of the centrifuge method for stability analysis of nanofluids. The instability profile and final instability index of binary nanofluids at different LiBr concentrations were illustrated in Fig. 11 and Table 4. According to Table 4, by increasing the concentration of LiBr, the instability index was increased

Light transmission of LiBr nanofluids at 50 wt.% of LiBr was shown in Fig. 12. The transmission curves of the formed LiBr nanofluids display a region of complete absorption, which indicates the formation of sediment under the centrifugation. The light transmission of all samples in Fig. 12 shows a polydisperse sedimentation pattern without observing any particle-particle agglomeration and flocculation [58]. However the intensity of sedimentation increases

for samples either at higher concentration of iron oxide or particles with large aspect ratios. The thin width regions of transmission curve imply high stability of samples for a long period of time. The zeta potential values of iron oxide nanofluid for different experimental runs with and without LiBr are presented in Table 3.

The zeta potential value of nanofluid is a measure of electrical double layer repulsion force between nanoparticles. Nanofluids with zeta potential between 40-60 mV have an acceptable stability by electrostatic repulsion [4]. Table 3 shows that the zeta potential of nanofluids after addition 30 wt.% LiBr salt decreases to a value between 1-3 mV. With more addition of LiBr salt (50 wt.%), the zeta potential decreases below 1 mV, which suggests the presence of thin and compressed double layers around nanoparticles. It can be concluded that the favorable functionalizing around iron nanoparticles (Fig. 2(c)) was provided by a strong steric repulsion between particles. In fact the low Hamaker constant, small size and good functionalizing of iron oxide nanoparticles made them stable in high ionic media of LiBr over several months. The TEM photo of iron oxide nanoparticles inside binary nanofluids (50 wt.% LiBr-Case 1) after six month's immobility is shown in Fig. 13. According to TEM photos of Fig. 13 any aggregation or corrosion has not been occurred for nanoparticles in LiBr solution. The visual observation of nanofluids after six months also have not shown any sedimentation for nanoparticles, which verified the long shelf-life of binary nanofluids (Fig. S5).

To confirm the dominant effect of steric stabilization, the interaction energy profiles for iron oxides nanoparticles were calculated using the DLVO theory for two same sized sphere-sphere geometries (Fig. 2(c)). The four major interaction energies of Van der Waals (W_{VdW}), steric repulsions (W_{steric}), magnetic attractions (W_M) and electrostatic double layer (W_{DL}) were considered. The correlations for estimation different interaction energy were provided in supplementary documents. All the parameter values used in the calculations are presented in Table 5. The predicted interaction energy between nanoparticles that stabilized by adsorbed double layer of surfactant in 50 wt% of LiBr salt is plotted in Fig. 14.

Fig. 14 clearly shows that the calculated value of the maximum W/kT for the DLVO profile is 20.01 kT, and the primary contribution is the steric repulsion. For low thermal barriers, i.e. < 5

kT, aggregation of nanopartiles is likely to occur [59]. However for our case, there is a sufficient energy barrier existing to prevent nanoparticles to form aggregation, and any weak aggregation should be disrupted by thermal motion as reflected by the strong stability, showing in Fig. 12.

Conclusion

In this study, stable iron oxide dispersions in LiBr/water were produced for many potential applications. The uniform spherical and rod shape nanoparticles were produced by the reverse microemulsion method. The morphological characterization showed that nanoparticles obtained with lower concentration were small, spherical and monodispersed, while the particles were converted to rod shape by increasing reactant concentration or the reaction temperature. An effective steric repulsion force was provided by the formation a double layer (admicelles) around the nanoparticles. The analysis of nanoparticles samples (i.e., TEM, visual observation and Lumisizer) in the presence of lithium bromide indicated an excellent stability over a long period of time (i.e.>6 months). The steric repulsion was determined as the main mechanism of the stability of nanoparticles, which was confirmed by the DLVO theory.

References

[1] W. J. Minkowycz, E. M. Sparrow, J. P. Abraham, Nanoparticle Heat Transfer and Fluid Flow, CRC Press, 2012.

[2] N. Sharma, H. Ojha, A. Bharadwaj, D. P. Pathakc, R. K. Sharma, RSC Adv., 5 (2015) 53381-53403.

[3] Z. Haddad, C. Abid, H.F. Oztop, A. Mataoui, Int. J. Therm. Sci. 76 (2014) 168-189.

[4] S. Mukherjee, S. Paria, IOSR-JMCE. 9 (2013) 63-69.

[5] M.A. Malik, M.Y. Wani, M.A. Hashim, Arab. J. Sci. Eng. 5 (2012) 397-417.

[6] G.D. Rees, R. Evans Gowing, S.J. Hammond, B.H. Robinson, Langmuir, 15 (1999) 1993-2002.

[7] J.N. Solanki, Z.V.P. Murthy, Colloids Surf. A. Physicochem. Eng. Asp. 359 (2010) 31-38.

[8] R. Latsuzbaia, E. Negro, G. Koper, Faraday Discuss. 181 (2015) 37-48.

[9] T. Alhawi, M. Rehan, D. York, X. Lai, Procedia Eng. 102 (2015) 346-355.

[10] K. Wongwailikhit, S. Horwongsakul, Mater. Lett. 65 (2011) 2820-2822.

[11] L.H. Han, H. Liu, Y. Wei, Powder Technol. 207 (2011) 42-46.

[12] J. Vidal-Vidal, J. Rivasb, M.A. Lopez-Quintelaa, Colloids Surf. A. Physicochem. Eng. Asp. 288 (2006) 44-51.

[13] R.J. Dossat T.J. Horan, Principles of Refrigeration Paperback, Prentice Hall, 5 ed., 2001.

[14] A. Elsafty, Solar Air Conditioning System: Water/Lithium Bromide Vapour Absorption system Perfect Paperback, Lap Lambert Academic Publishing, 2013.

[15] H. Zhang, H.J. Chen, X. Du, D. Wen, Sol. Energy. 100 (2014) 141-147.

[16] S.C. Alfaro, S. Lafon, J.L. Rajot, P. Formenti, A. Gaudichet, J. Geophys. Res. 109 (2004) 1-9.

[17] M. Sesen, Y. Teksen, B. Sahin, K.t Sendur, M.P. Menguc, A. Kosar, Appl. Phys. Lett. 102 (2013) 163107.

[18] M. Shojaeian, M.M. Yildizhan, O. Coskun, E. Ozkalay, Y. Teksen, M.A. Gulgun, H.F.Y. Acar, A. Kosar, Materials Res. Exp., 3 (2016) 096102.

[19] W. Wu, Z. Wu, T. Yu, C. Jiang, W. Kim, Sci. Technol. Adv. Mater. 16 (2015) 1-43.

[20] J.K. Lim, S.A. Majetich, R.D. Tilton, Langmuir, 25 (2009) 13384-13393.

[21] E. Nourafkan, A. Alamdari, Ind. Eng. Chem. 20 (2014) 3639-3645

[22] R. Massart, IEEE Trans. Magn. 17(1981) 1247-1248.

[23] K. Mandel, F. Hutter, Nano Today. 7 (2012) 485-487.

[24] R.A. Sperling, W.J. Parak, Phil. Trans. R. Soc. A. 368 (2010) 1333-1383.

[25] H. Kim, J. Jeong, and Y. Tae, Int. J. Refrig. 35 (2011) 645-651.

[26] J. Y. Jung, E.S. Kim, Y. Nam, Y.T. Kang, Int. J. Refrig. 36 (2013) 1056-1061.

[27] C.W. Liao, J.H. Yu, Y.S. Tarng, On-line full scan inspection of particle size and shape using digital image processing, Particuology. 8 (2010) 286-292.

[28] G. H. A. Janaka, J. Kumara, K. Hayano, Keita Ogiwara, Image Analysis Techniques on Evaluation of Particle Size Distribution of Gravel, J. Geomate. 3 (2012) 290-297.

[29] L.C. Gontard, D. Ozkaya, R.E. Dunin-Borkowski, Ultramicroscopy 111 (2011) 101-106.

[30] C.C. Chen, C.K. Yu, Mater. Chem. Phys. 85 (2004) 227–237.

[31] B. Vogel, H. Siebert, U. Hofmann, S. Frantz, MethodsX. 2 (2015) 124–134.

[32] F. Cappia, D. Pizzocri, A. Schubert, P. Van Uffelena, G. Paperinia, D. Pellottieroa, R. Macian-Juanb, V.V. Rondinellaa, J. Nucl. Mater. (2016) 138-149.

[33] H. Jin, G. Lin, L. Bai, A. Zeiny, D. Wen, Nano Energy, 2016.

[34] A. Samodi, A. Rashidi, K. Marjani, S. Ketabi, Mater. Lett. 109 (2013) 269-274.

[35] M. Grzelczak, J. Perez-Juste, P. Mulvaney, L.M. LizMarzan, Chem. Soc. Rev. 37 (2008) 1783-1791.

[36] N. Moloto, N. Revaprasadu, P.L. Musetha, M.J. Moloto, J. Nanosci. Nanotechnol. 9 (2009) 4760-4766.

[37] O.A. Yildirim, C. Durucan, J. Alloys Compd. 506 (2010) 944-949.

[38] C.Y. Chiu, Y. Li, L. Ruan, X. Ye, C.B. Murray, Y. Huang, Nat. Chem. 3 (2011) 393-399.

[39] T.J. Zhu, X. Chen, X.Y. Meng, X.B. Zhao, J. He, Cryst. Growth Des. 10 (2010) 3727-3731.

[40] S. Bhattacharya, j. Biswas, Nanoscale. 3 (2011) 2924-2930.

[41] C. Palache, H. Berman, C. Frondel, Dana's System of Mineralogy, New York, Wiley, (1944).

[42] C. Han, J. Ma, H. Wu, Y.Wei ,K. Hu, Chil. Chem. Soc. 59 (2015) 2248-2251.

[43] Y. Ding, J.R. Morber, R.L. Snyder, Z.L. Wang, Adv. Funct. Mater. 17 (2007) 1172-1178.

[44] H. Wiogo, M. Lim, P. Munroe, R. Amal, Cryst. Growth. Des. 11 (2011) 1689-1696.

[45] J. Li , Y. Pan, Q. Liu, K. Yu-Zhang, N. Menguy, R. Che, H. Qin, W. Lin, W. Wu, N. Petersen, X. Yang, Earth Planet. Sci. Lett. 293 (2010) 368-376.

[46] C.T. Lefevre , M. Posfai , F. Abreu , U. Lins , R.B. Frankel , D.A. Bazylinski, Earth Planet. Sci. Lett. 312 (2011) 194-200.

[47] U. Lins, M.R. McCartney, M. Farina, R. B. Frankel, P.R. Buseck, Appl. and environ. Microbial. 71 (2005) 4902-4905.

[48] K.L. Thomas-Keprta, S.J. Clemett, D.A. Bazylinski, J.L. Kirschvink, D.S. McKay, S.J. Wentworth, H. Valii, E.K. Gibson, M.F. McKay, C.S. Romanek, PNAS, 98 (2001) 2164-2169.

[49] J. Wang, Z. Peng, Y. Huang, Q. Chen, J. Cryst. Growth. 263 (2004) 616-619

[50] S. Mathur, S. Barth, U. Werner, F. Hernandez-Ramirez, A. Romano-Rodriguez, Adv. Mater. 20 (2008) 1550-1554.

[51] S. B. Gogoi, K. Hazarika, R. Phukan, P. Tiwari, R. Uppaluri, A. Rajbongshi, AICHE Annual Meeting, Salt Lake City, 2015.

[52] M.S. Bakshi, J. Singh, K. Singh, G. Kaur, Colloids Surf. A. Physicochem. Eng. Asp. 234 (2004) 77-84.

[53] A. Bera, K. Ojha, A. Mandal, J. Surfactants Deterg. 16 (2013) 621-630.

[54] P. Posocco, A. Perazzo, V. Preziosi, E. Laurini, S. Pricl, S. Guido, RSC Adv. 6 (2016) 4723.

[55] X. Li, W. Zheng, G. He, R. Zhao, D. Liu, ACS Sustainable Chem. Eng. 2 (2014) 288-295.

[56] J. Walter, T. Thajudeen, S. Sub, D. Segetsa, W. Peukert, Nanoscale. 7 (2015) 6574-6587.

[57] H.T. Chiu, C.Y. Chang, T.Y. Chiang, M.T. Kuo, Y.H. Wang, J. Polym. Res. 18 (2011) 1587-1596.

[58] B. Schluter, R. Mulhaupt, A. Kailer, Tribol. Lett. 53 (2014) 353-363.

[59] Y. Wang, R.J. Pugh, E. Forssberg, Colloids Surf. A. Physicochem. Eng. Asp. 90 (1994) 117-133.

[60] B. Faure, G. Salazar-Alvarez, L. Bergstroom, Langmuir. 27 (2011) 8659-8664.

[61] R.C. Wheast, Handbook of Chemistry and Physics, 64th ed. CRC Press, Florida, 1984.

[62] T. Hattori, Cleaning and Surface Conditioning Technology in Semiconductor, published by the Electrochemical Society, Issue 2, 2009.

[63] L.W. Nichol, A. G. Ogston, B. N. Preston, J. Biochem. 102 (1967) 407-416.

[64] J. K. Lim, S. A. Majetich, R. D. Tilton, Langmuir. 25 (2009) 13384-13393.

[65] J. Rosen, Permeability (Physics), Encyclopedia of Physics, Facts on File science library, New York, 2004.

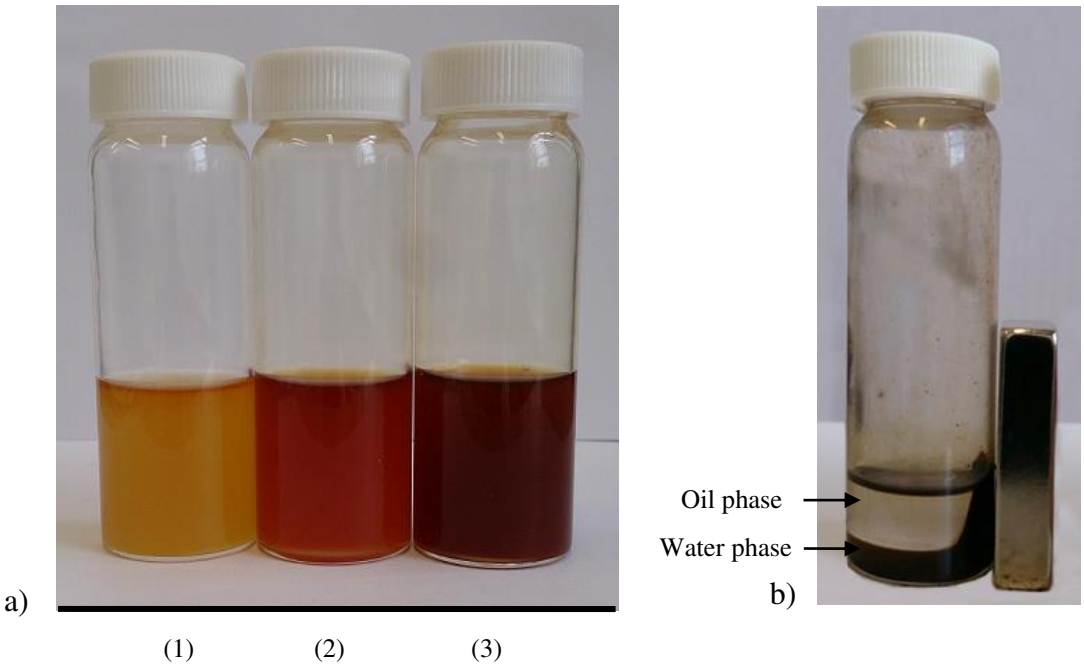

Fig. 1. The final dispersions of different experimental runs (a-1) Case 1 (a-2) Case 2 (a-3) Case 3 and (b) sample run without using any surfactant.

a)

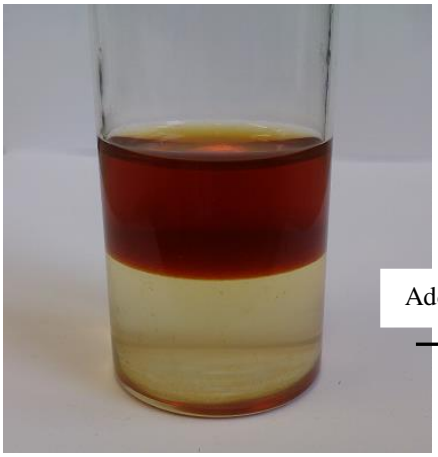

Addition of acid citric

b)

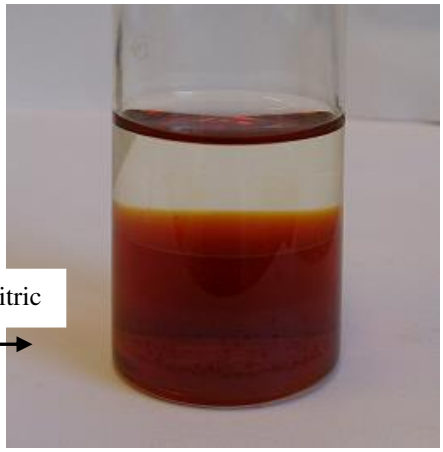

c)

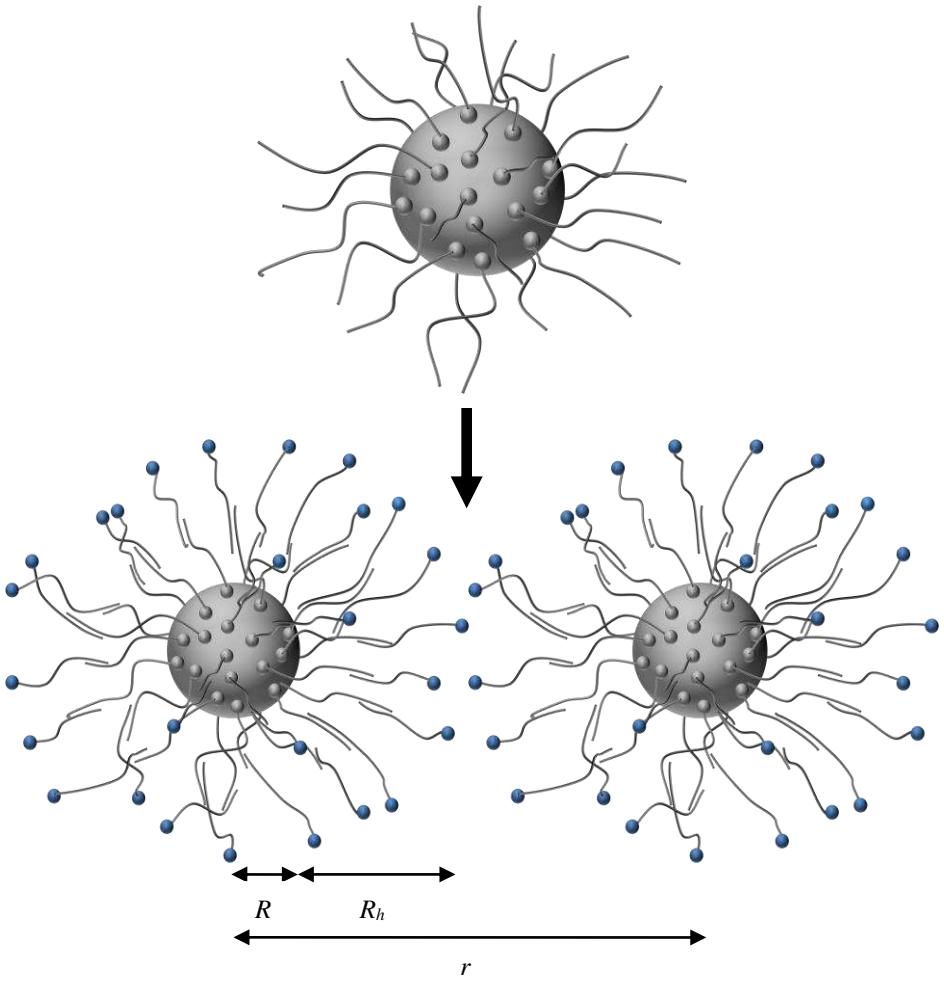

Fig. 2. (a, b) phase transformation of Fe_3O_4 nanoparticle from an organic phase to an aqueous phase, and (c) the proposed mechanism for formation new ligand around particles during phase transformation inferred from the DLS analysis (R: particle radius, R_h: thickness of the absorbed admicell layer of surfactant, r: distance of center to center of particles).

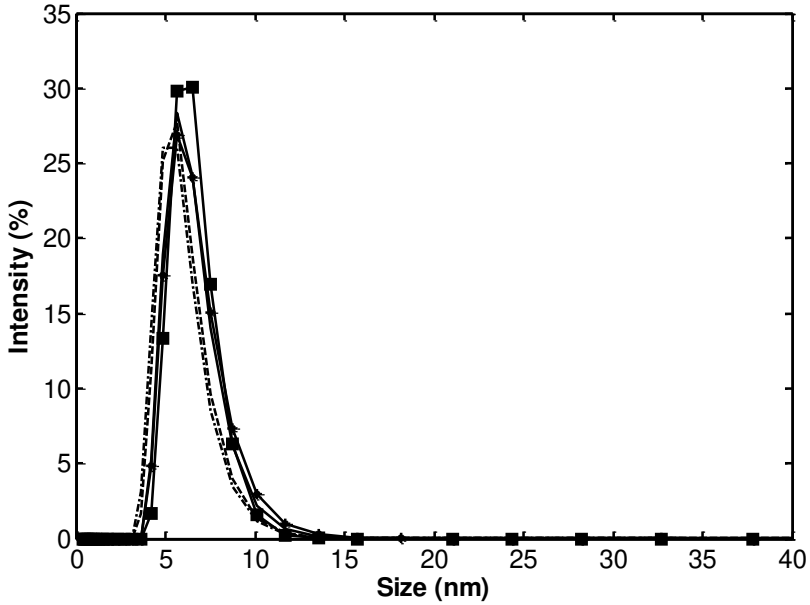

a)

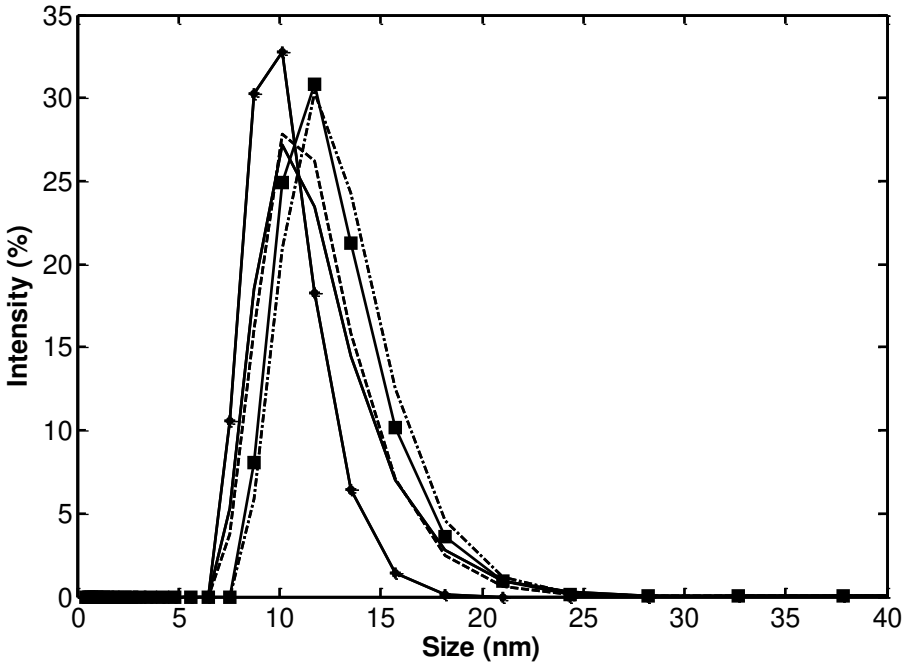

b)

Fig. 3. Particle size distribution of Fe_3O_4 nanoparticle using DLS for Case 2 (a) in cyclohexane phase (b) after addition of acid citric and phase transfer.

(1) (2) (3) (4) (5) (6)

Fig. 4. The final nanofluid of different experimental runs (1) Case 1 (2) Case 4 (3) Case 2 (4) Case 5 (5) Case 3 (6) Case 6.

a)

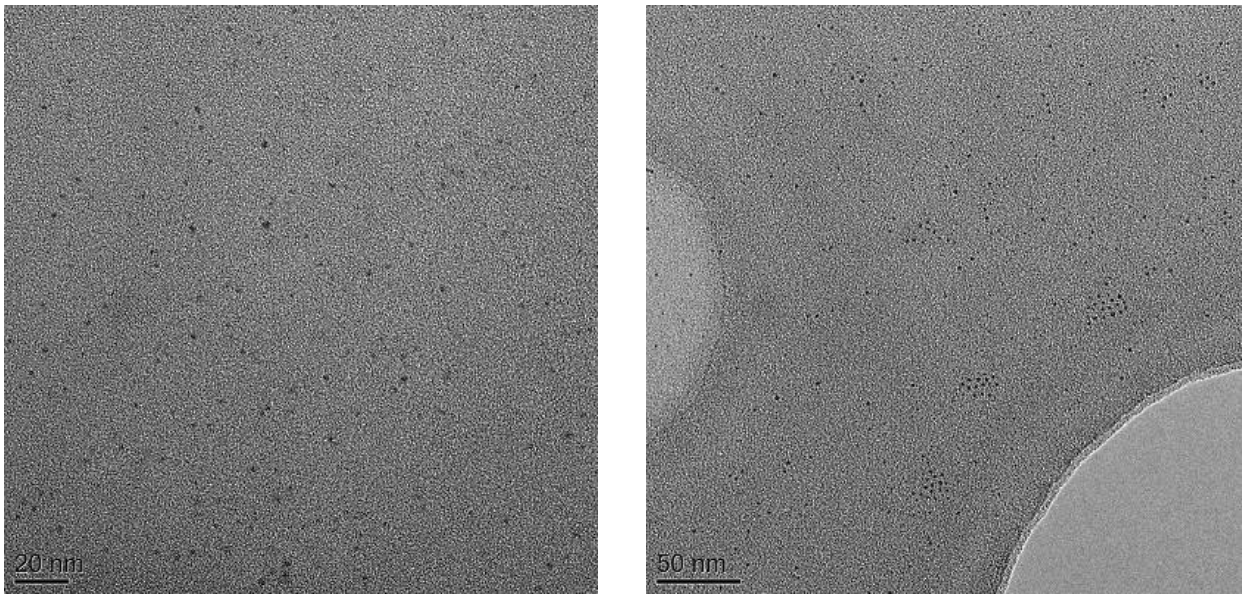

b)

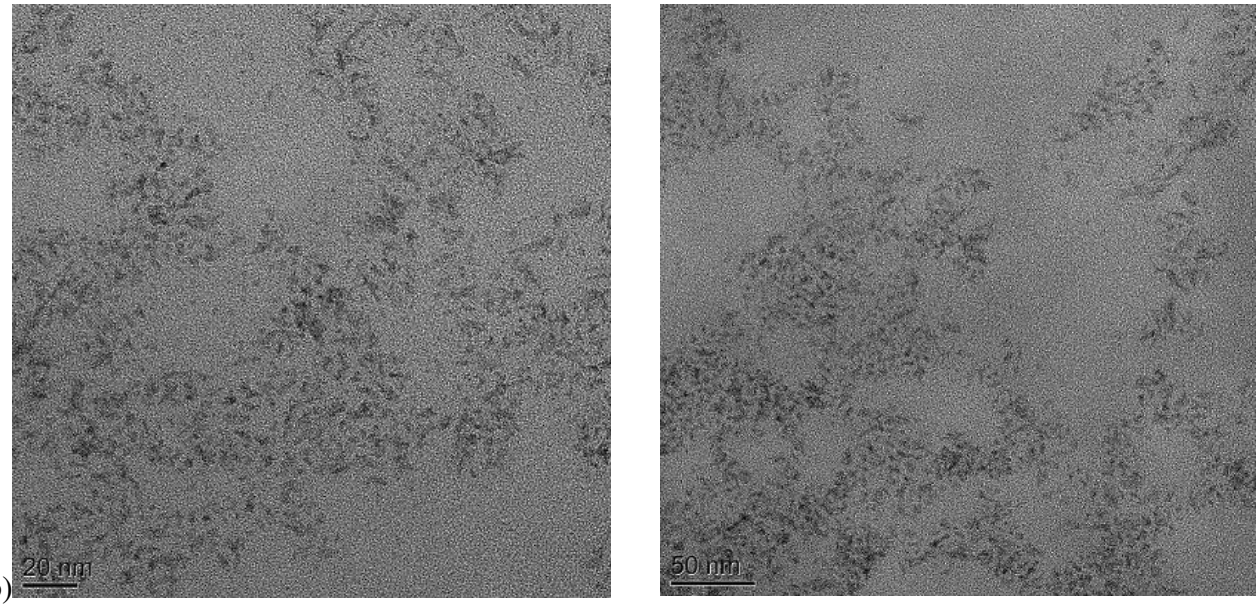

c)

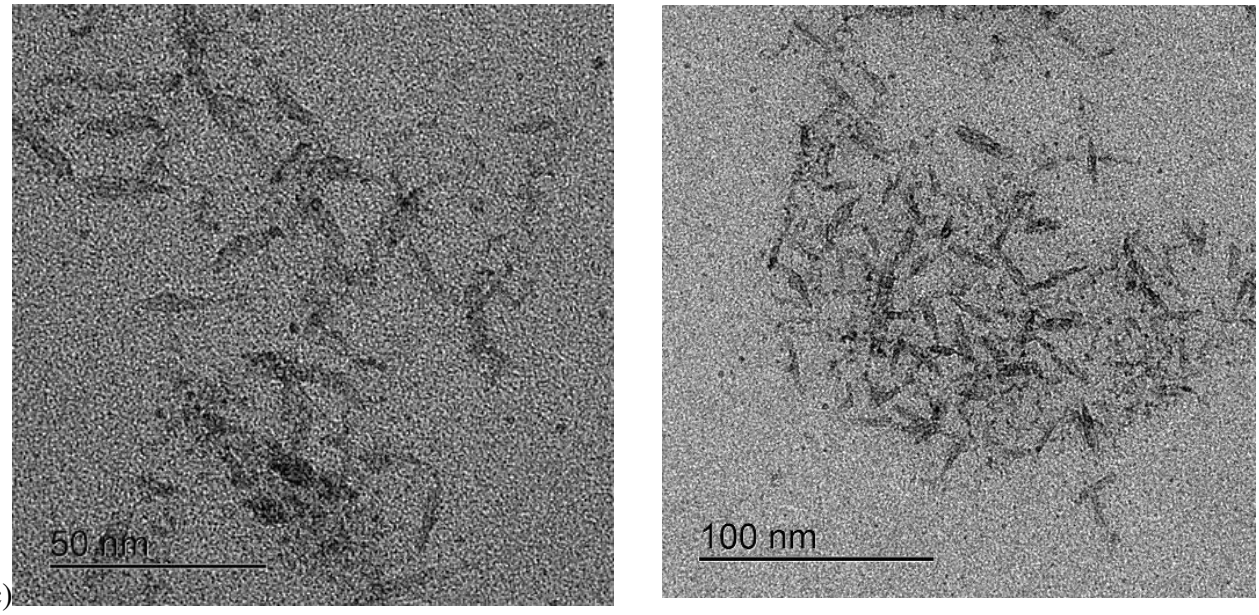

d)

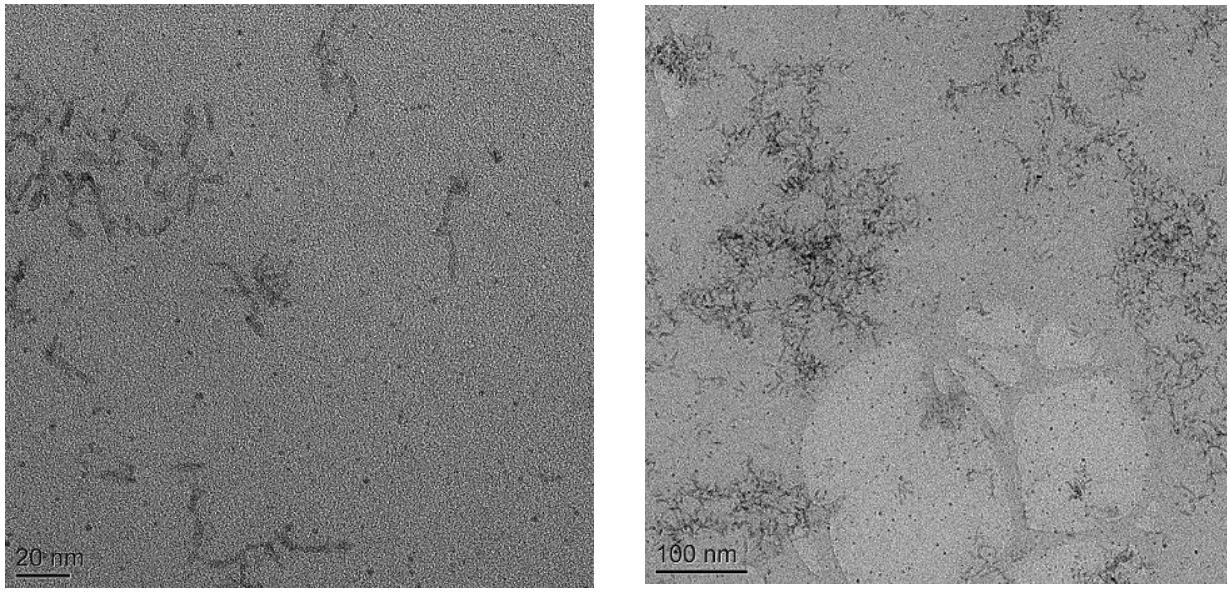

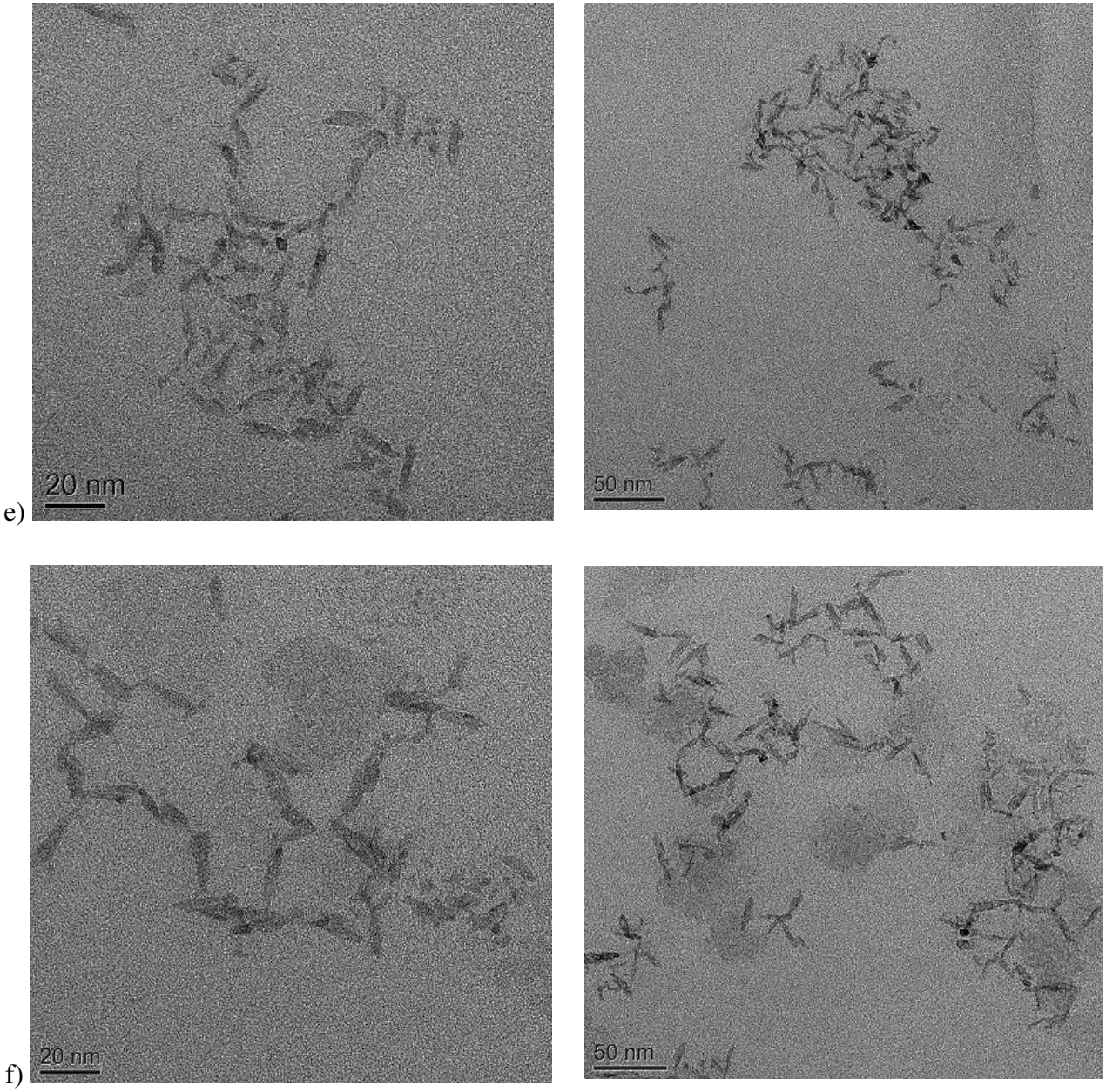

Fig. 5. TEM images of different experimental runs (a) Case 1 (b) Case 2 (c) Case 3 (d) Case 4 (e) Case 5 (f) Case 6.

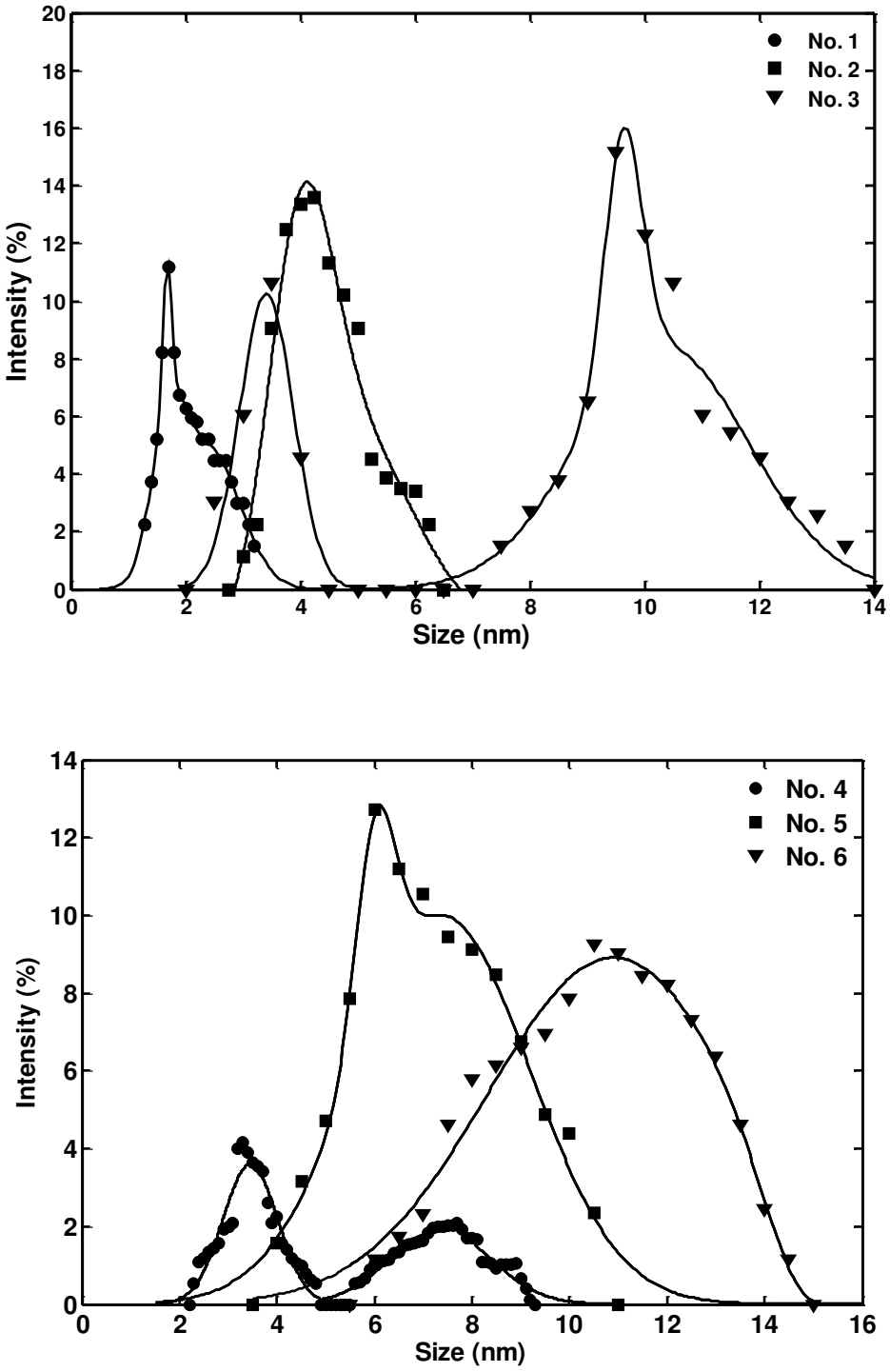

Fig. 6. The particle size distribution of nanofluids was estimated by analyzing of TEM photos at least for 100 nanoparticles.

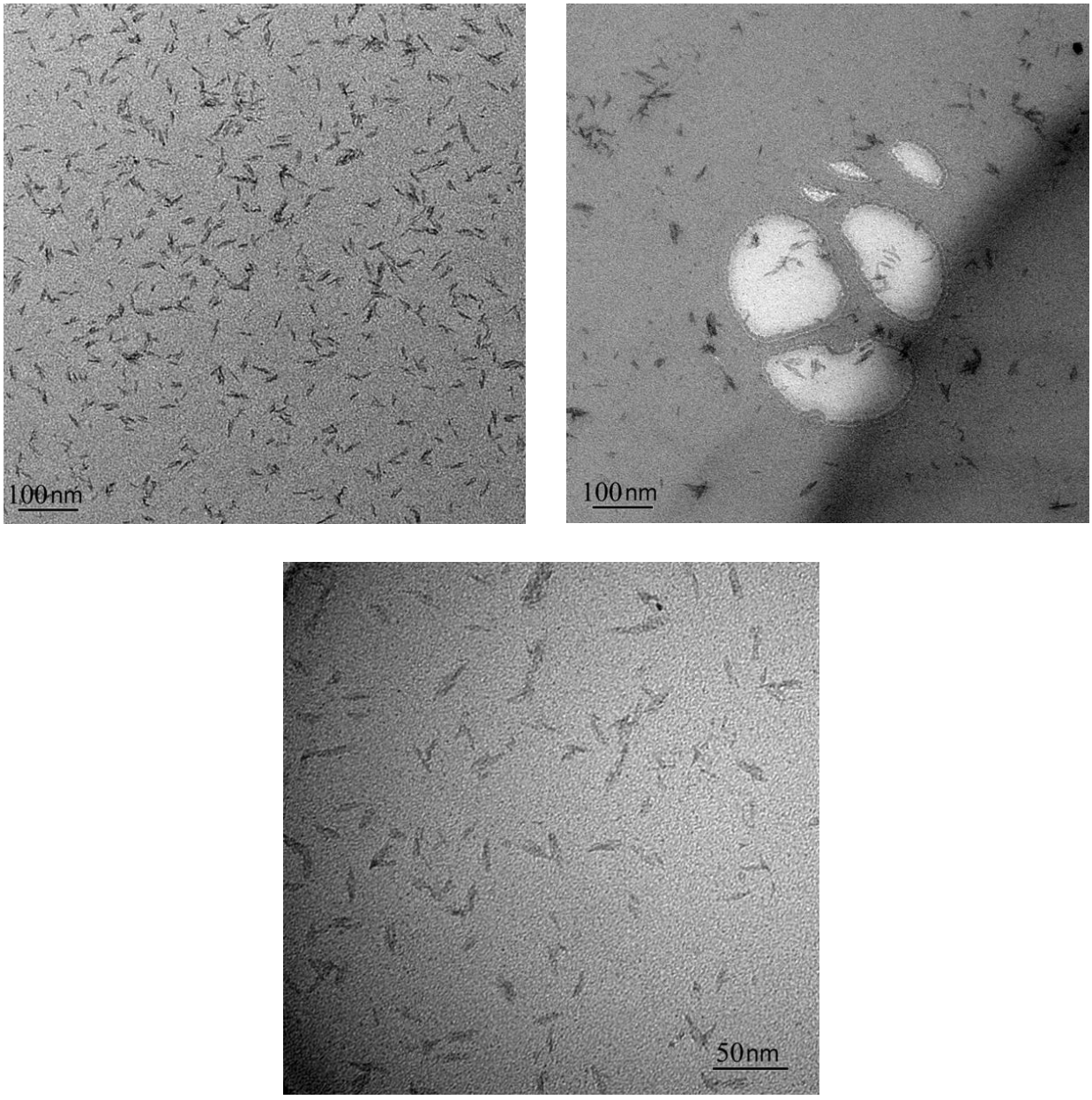

Fig. 7. (a) TEM image (b) hydrodynamic size and (c) stability analysis of nanoparticles which was synthesized using recovered oil phase.

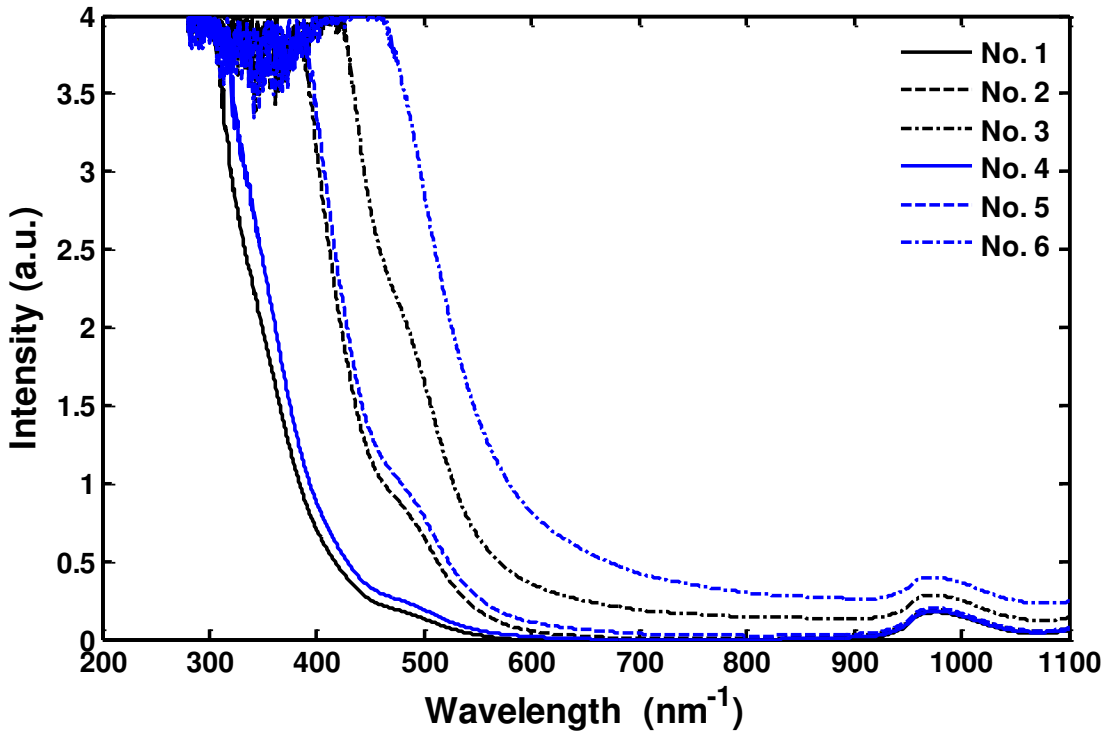

Fig. 8. UV-vis absorption spectra of Fe_3O_4/water nanofluids with normalized absorbance.

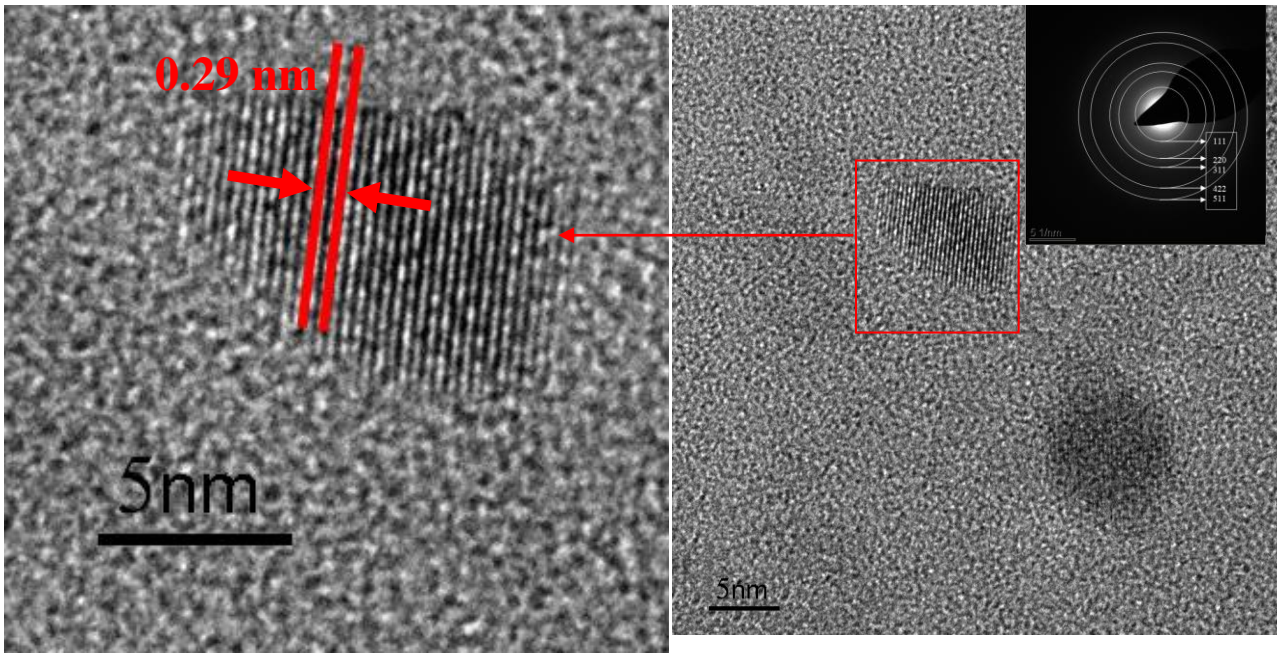

a)

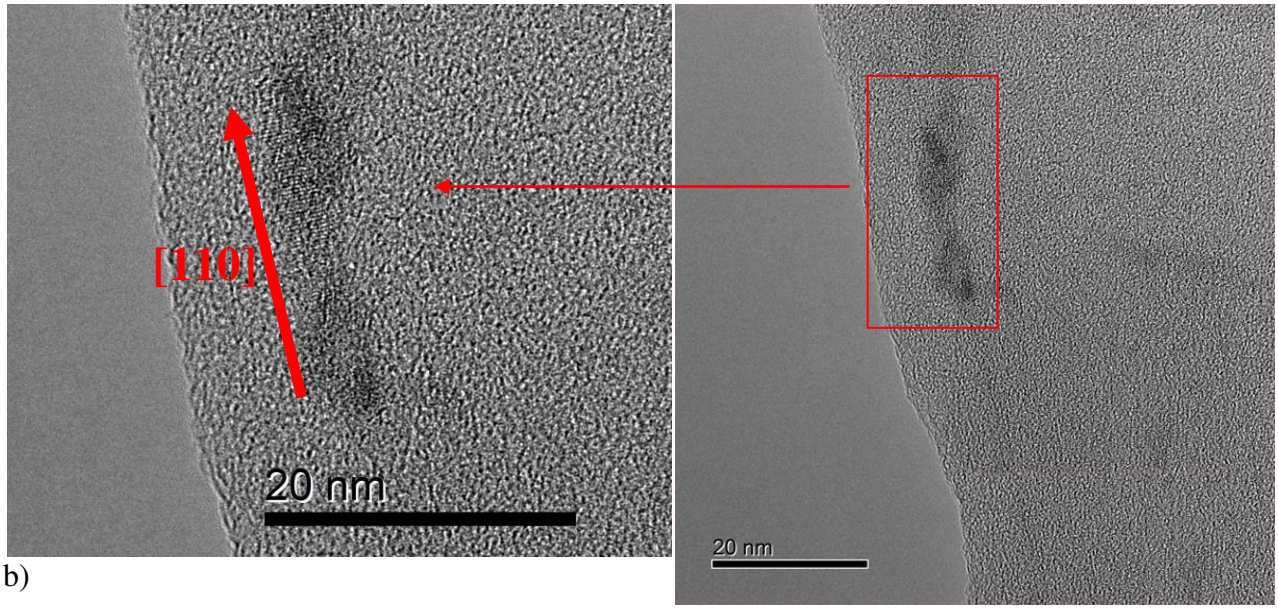

b)

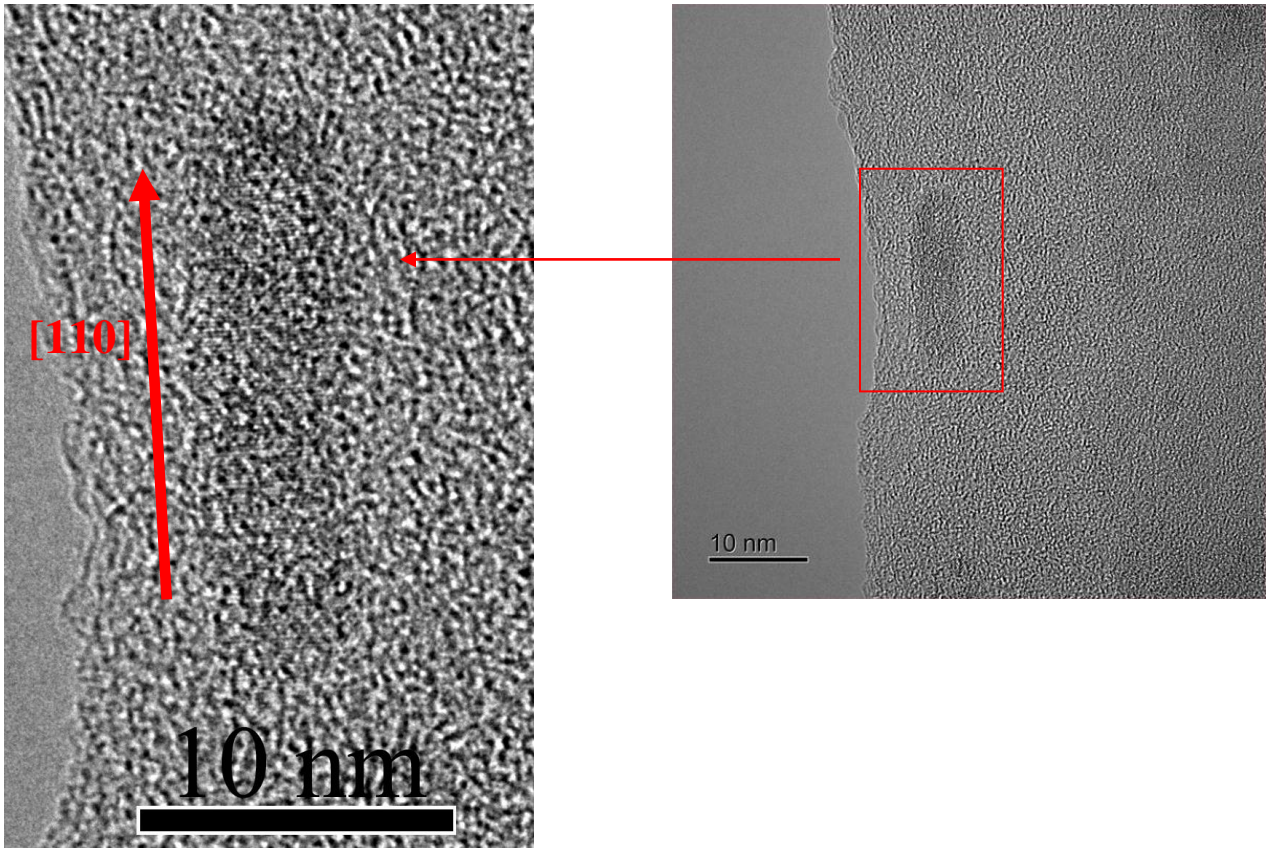

c)

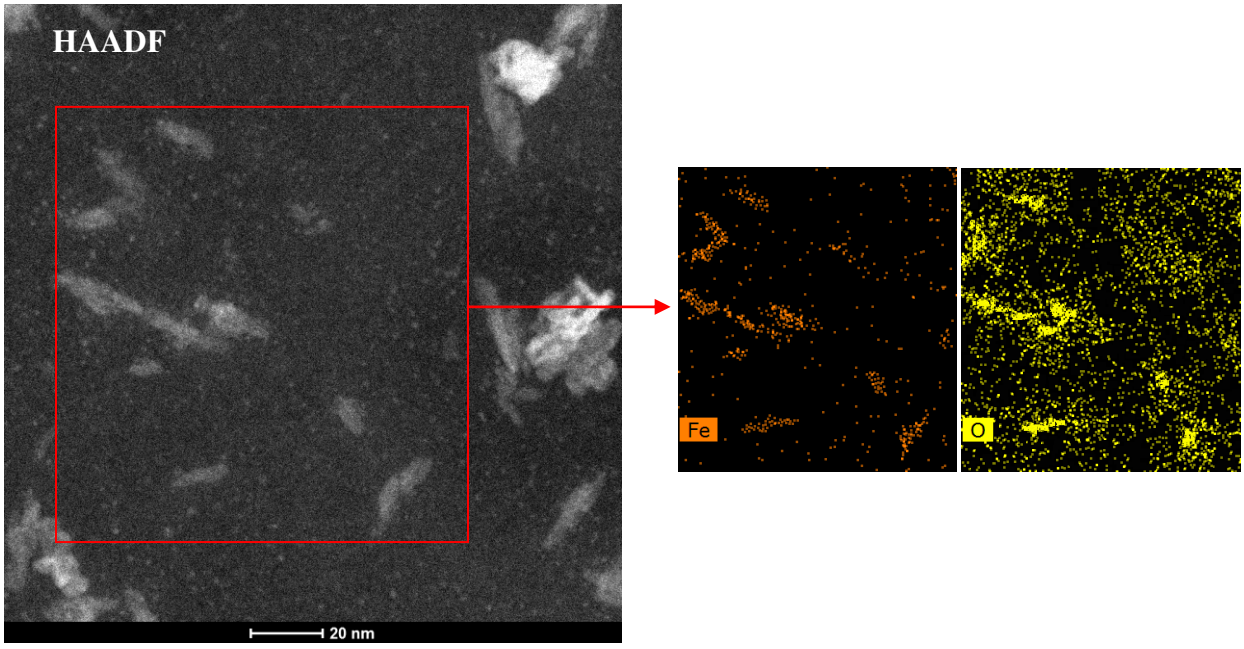

d)

e)

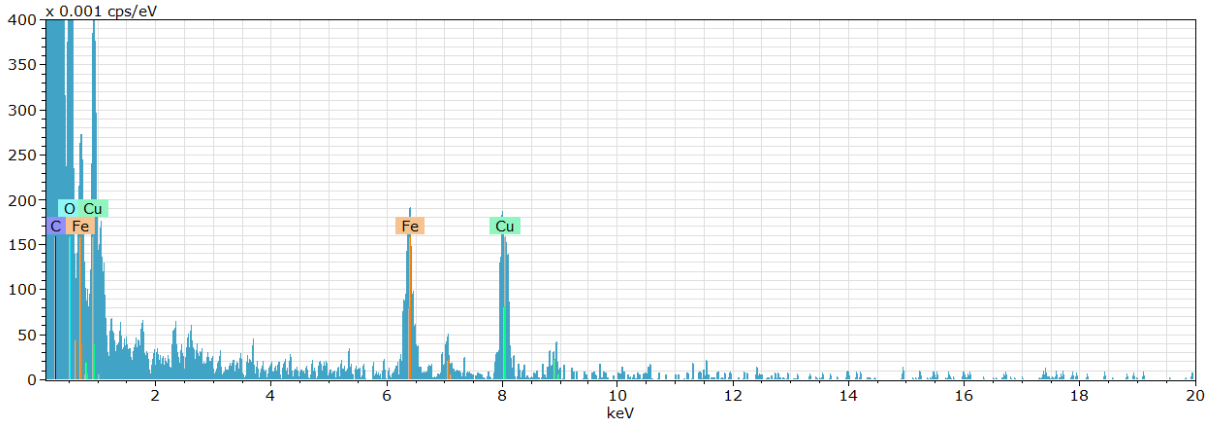

Fig. 9. Spherical nanoparticles HRTEM (a), rod shaped nanoparticles HRTEM (b, c) HAADF image, elemental map (d) and EDEX (e) analysis of rod shape nanoparticles.

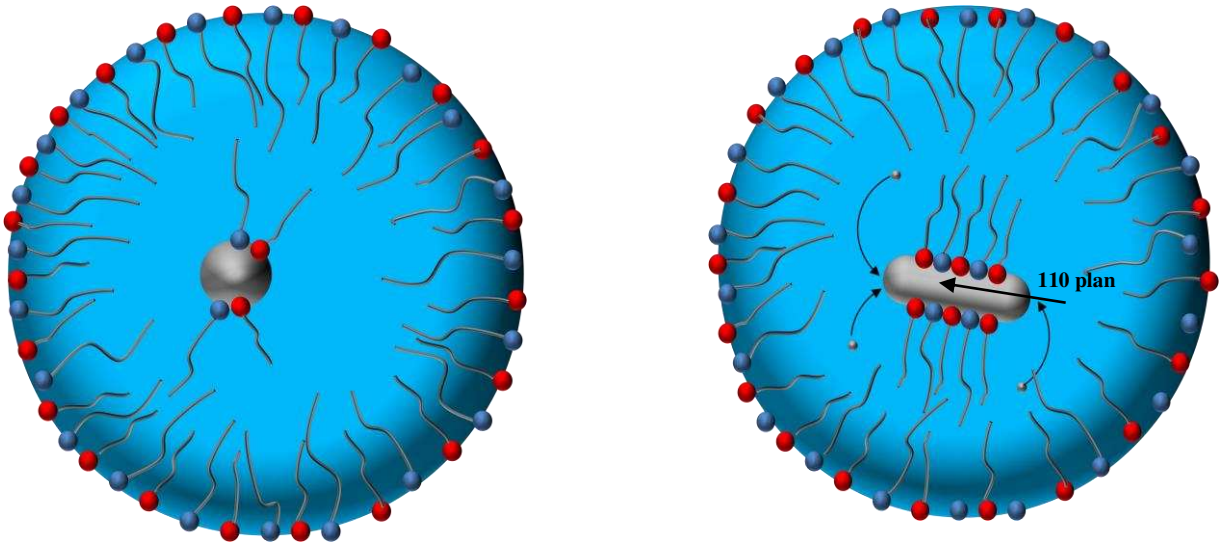

a)

b)

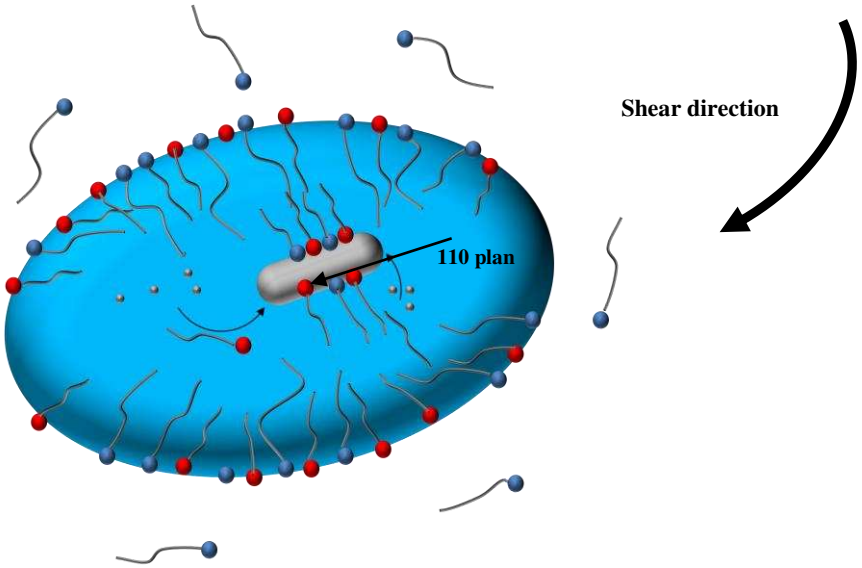

c)

Tween molecule

Span molecule

Fig. 10. Proposed mechanism of iron oxide nanoparticles formation inside droplet at (a) low reactant concentration (b) high reactant concentration (c) at elevated temperature.

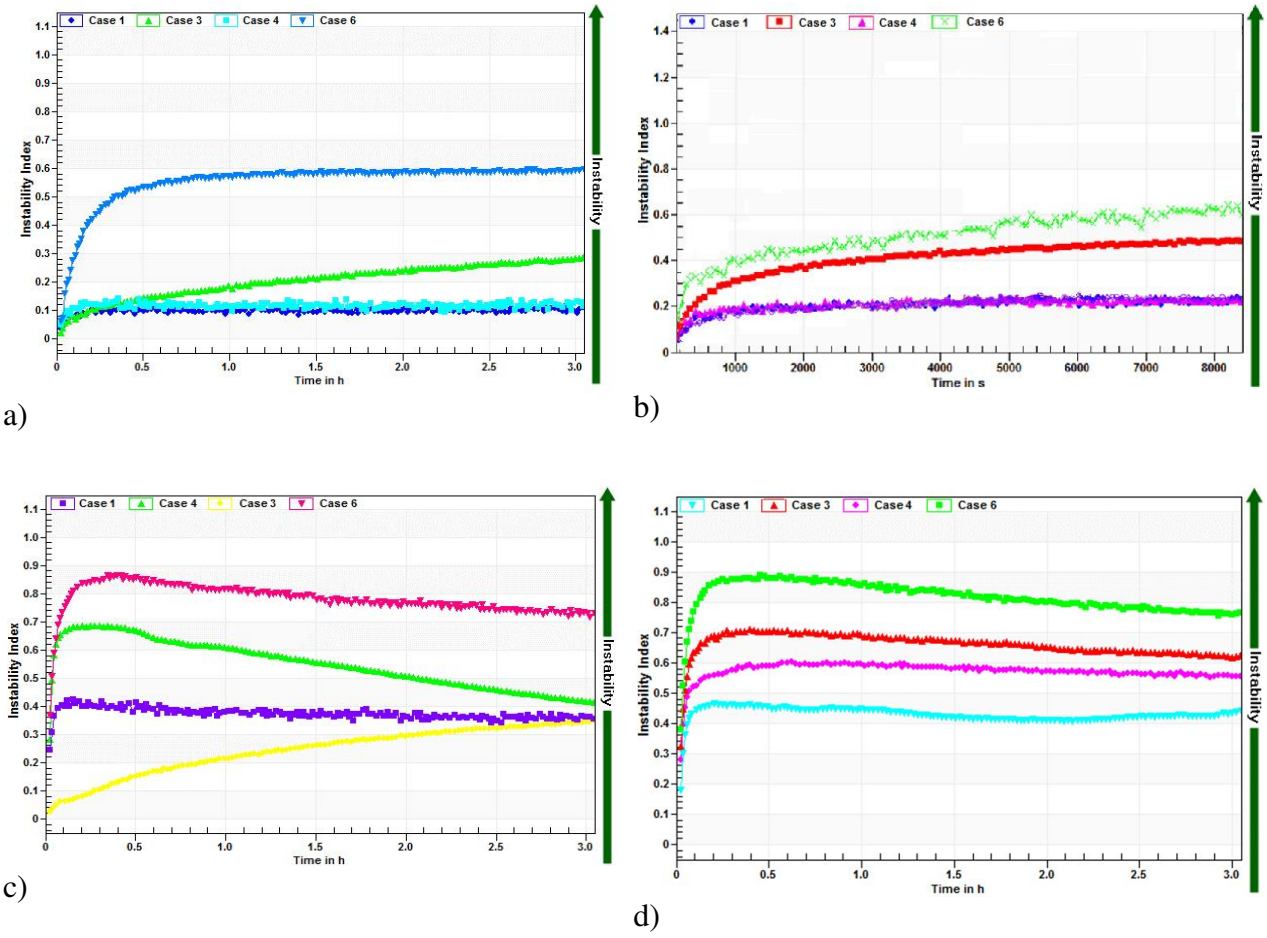

Fig. 11. Instability profile of binary nanofluids at different LiBr concentration (a) 20 wt.% (b) 30 wt.% (c) 40 wt.% (d) 50 wt.%.

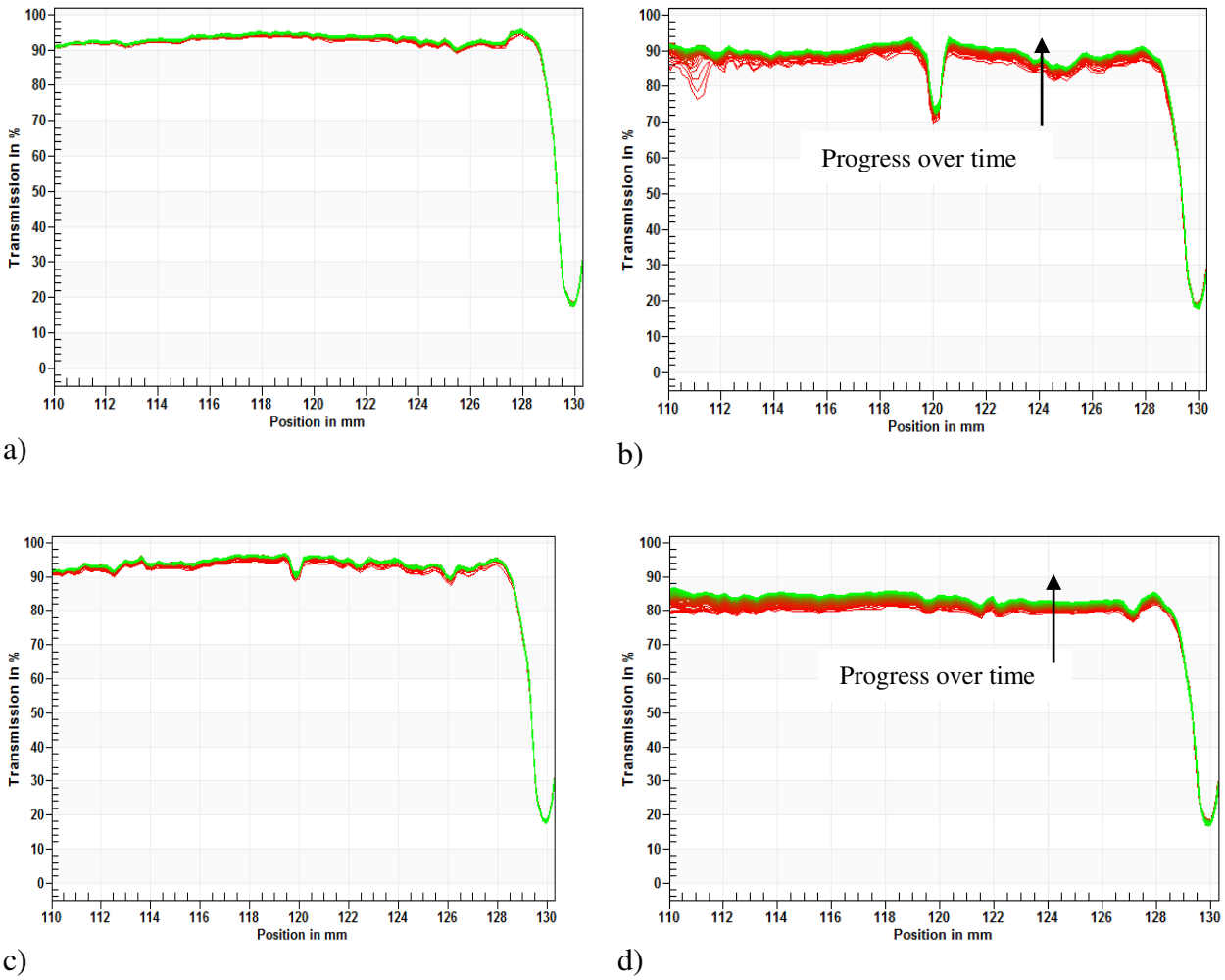

Fig. 12. Light transmission of LiBr nanofluids (a) Case 1 (b) Case 3 (c) Case 4 (d) Case 6.

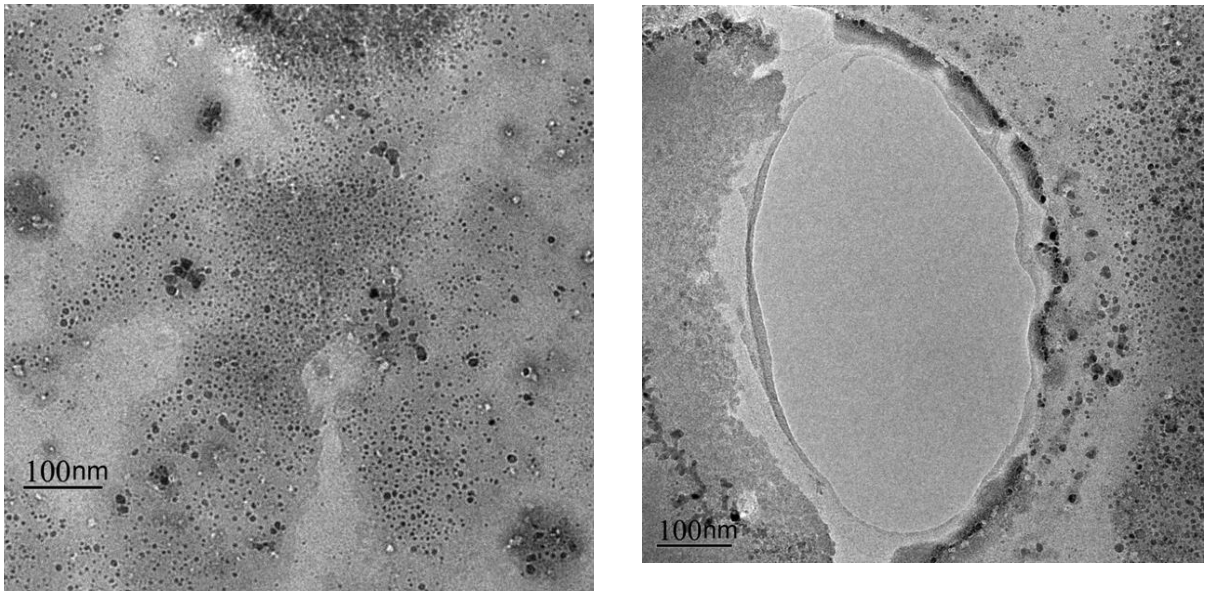

Fig. 13. TEM photo of iron oxide nanoparticles inside binary nanofluids (50 wt.% LiBr-Case 1) after six month immobility.

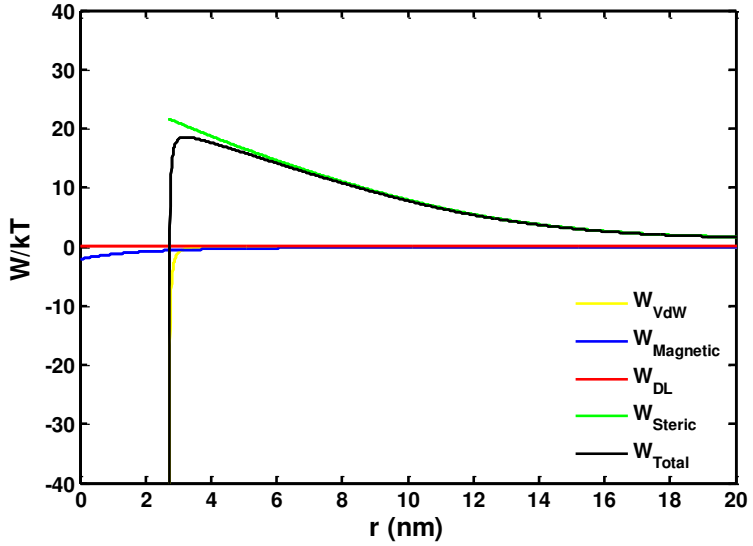

Fig. 14. Predicted potential energy profiles of DLVO for sphere-sphere geometries of iron oxide nanoparticles.

Table 1. The condition of nanoparticle synthesis in different experiment runs.

Experimental run number	Ferrous chloride molarity	Temperature
Case 1	0.01	22 ℃ (Room)
Case 2	0.05	22 ℃
Case 3	0.1	22 ℃
Case 4	0.01	70 ℃
Case 5	0.05	70 ℃
Case 6	0.1	70 ℃

Table 2. The characterization of nanoparticle for different experiment runs.

Experimental No	Morphology	Average size	Concentration (ppm)	Polydispersity index	Aspect ration of rod nanoparticles
Case 1	**Spherical**	2.1	55±7	0.059	1
Case 2	**Spherical**	5.4	288±11	0.029	1
Case 3	**Mix Spherical/Rod**	8.5	594±27	0.161	-
Case 4	**Mix Spherical/Rod**	3.6	61±4	0.263	-
Case 5	**Rod**	7.3	306±24	0.042	2.66
Case 6	**Rod**	13.3	618±14	0.070	3.41

Table 3.The zeta potential of different nanofluids with and without 50 wt.% lithium bromide and repeatability of instability index.

	ζ (mV)			Final instability index (0 wt.% LiBr)
Experimental run number	**In absence of LiBr**	**In presence of 30 wt.% LiBr**	**In presence of 50 wt.% LiBr**	
Case 1	-10.56±0.15	-0.88±0.031	-0.17±0.071	0.0993±0.018
Case 3	-9.6±0.27	-2.48±0.063	-0.14±0.06	0.225±0.016
Case 4	-12.06±0.14	-1.02±0.013	-0.86±0.07	0.117±0.026
Case 6	-12.82±0.22	-3.11±0.21	-0.29±0.07	0.28±0.009

Table 4. Final instability index of binary nanofluids at different LiBr concentration.

Experimental run number	Final instability index (20 wt.% LiBr)	Final instability index (30 wt.% LiBr)	Final instability index (40 wt.% LiBr)	Final instability index (50 wt.% LiBr)
Case 1	0.1033	0.2375	0.3575	0.4376
Case 3	0.2820	0.4858	0.4137	0.6242
Case 4	0.1259	0.2300	0.3419	0.5542
Case 6	0.5911	0.6388	0.7235	0.7556

Table 5. Parameter values used in the calculation of the DLVO interaction energy profiles.

Parameters	Unit	Value	Reference
R	*nm*	2.7	This study
R_h	*nm*	6.3	This study
r	*nm*	12.6	This study
A_{IO}	*J* ($kg.m^2s^{-2}$)	30×10^{-21}	[60]
k	$J.K^{-1}$	1.38×10^{-23}	[61]
T	*K*	277	This study
σ_p	$Molecule.nm^{-2}$	0.5	[62]
ρ_p	$g.ml^{-1}$	1.62	This study
M_w	$g.mol^{-1}$	1221	This study
χ	-	0.485	[63]
M_s	$A.m^{-1}$	2.86×10^{5}	[64]
μ_0	$m.kg.s^{-2}.A^{-2}$	1.26×10^{-6}	[65]
ε_0	$s^4A^2m^{-3}kg^{-1}$	8.854×10^{-12}	[61]
ε_R	-	78.5	[61]
ζ	$kgm^2s^{-3}A^{-1}$	Table 3	This study
e	A.s	1.602×10^{-19}	[61]
v	nm^3	0.0289	-
ϕ_p	-	0.12	This study
N_A	mol^{-1}	6.02×10^{23}	[61]